J. Fluid Mech. (1990), *vol.* 216, *pp.* 71–91
Printed in Great Britain

The transition from two-dimensional to three-dimensional planforms in infinite-Prandtl-number thermal convection

By BRYAN TRAVIS[1], PETER OLSON[2]
AND GERALD SCHUBERT[3]

[1] Earth and Space Sciences Division, Los Alamos National Laboratory, Los Alamos, NM 87545, USA

[2] Department of Earth and Planetary Sciences, The Johns Hopkins University, Baltimore, MD 21218, USA

[3] Department of Earth and Space Sciences, University of California, Los Angeles, CA 90024, USA

(Received 11 January 1989 and in revised form 28 November 1989)

The stability of two-dimensional thermal convection in an infinite-Prandtl-number fluid layer with zero-stress boundaries is investigated using numerical calculations in three-dimensional rectangles. At low Rayleigh numbers ($Ra < 20000$) calculations of the stability of two-dimensional rolls to cross-roll disturbances are in agreement with the predictions of Bolton & Busse for a fluid with a large but finite Prandtl number. Within the range $2\times10^4 < Ra \leqslant 5\times10^5$, steady rolls with basic wavenumber $\alpha > 2.22$ (aspect ratio < 1.41) are stable solutions. Two-dimensional rolls with basic wavenumber $\alpha < 1.96$ (aspect ratio > 1.6) are time dependent for $Ra > 4\times10^4$. For every case in which the initial condition was a time-dependent large-aspect-ratio roll, two-dimensional convection was found to be unstable to three-dimensional convection. Time-dependent rolls are replaced by either bimodal or knot convection in cases where the horizontal dimensions of the rectangular box are less than twice the depth. The bimodal planforms are steady states for $Ra \leqslant 10^5$, but one case at $Ra = 5\times10^5$ exhibits time dependence in the form of pulsating knots. Calculations at $Ra = 10^5$ in larger domains resulted in fully three-dimensional cellular planforms. A steady-state square planform was obtained in a $2.4\times2.4\times1$ rectangular box, started from random initial conditions. Calculations in a $3\times3\times1$ box produced steady hexagonal cells when started from random initial conditions, and a rectangular planform when started from a two-dimensional roll. An hexagonal planform started in a $3.5\times3.5\times1$ box at $Ra = 10^5$ exhibited oscillatory time dependence, including boundary-layer instabilities and pulsating plumes. Thus, the stable planform in three-dimensional convection is sensitive to the size of the rectangular domain and the initial conditions. The sensitivity of heat transfer to planform variations is less than 10%.

1. Introduction

We present results of numerical calculations of three-dimensional, time-dependent, infinite-Prandtl-number thermal convection in a rectangular box with free-slip boundaries, which is heated from below and cooled from above, for Rayleigh numbers $Ra \leqslant 5\times10^5$. The objectives are to determine the stability of two-dimensional rolls to three-dimensional disturbances at Rayleigh numbers far above the critical value, and to establish the preferred three-dimensional planforms when two-dimensional flows are unstable. Rayleigh–Bénard convection in an infinite-Prandtl-number incompressible fluid is the simplest fluid mechanical analogue to thermal convection in the Earth's mantle. This model system represents an extreme idealization of mantle convection, since it does not include many of the effects that are important in subsolidus mantle convection, including sphericity, variable rheology, internal heat production and compressibility. It is nevertheless an interesting case to study for several reasons. Most of the numerical experiments in the literature which are purported to be realistic simulations of mantle convection in fact resolve only two dimensions of motion, whereas flow in the mantle is in fact three-dimensional. It is therefore important to determine the effects that arise solely from adding the third dimension, without additional complications present. This is most easily done in the context of the classical problem of Rayleigh–Bénard convection in a homogeneous fluid, for which the structure of two-dimensional flow is well established. In addition, the practical difficulties associated with producing free-slip boundaries has discouraged experimental work on this problem. As a result, the three-dimensional structure of infinite-Prandtl-number convection between stress-free plane boundaries at high Rayleigh numbers is still largely undetermined.

The changes in flow structure in a thermally convecting, high-Prandtl-number fluid with rigid and isothermal horizontal plane boundaries is well known from both analytical studies (Busse 1967*a*) and experiment (Busse & Whitehead 1971; Whitehead & Parsons 1978). Two-dimensional convection rolls are the stable planform only over a limited range of horizontal wavenumbers (or cell aspect ratios) and more importantly only over a limited range of Rayleigh numbers. Above $Ra = 2\times10^4$, two-dimensional rolls with arbitrary wavenumber are replaced by steady bimodal convection consisting of a superposition of two orthogonal sets of rolls, which are in turn replaced at larger Rayleigh numbers by time-dependent, three-dimensional flow. In contrast, much less is known of the behaviour of the same system when the horizontal boundaries are zero-stress surfaces. Stability analyses of Rayleigh–Bénard convection with free-slip boundaries by Straus (1972) and by Bolton & Busse (1985) demonstrated that two-dimensional rolls with wavenumbers near the critical value are stable to infinitesimal three-dimensional disturbances up to $Ra = 2\times10^4$ in an infinite-Prandtl-number fluid. At large but finite Prandtl number, the Rayleigh number–wavenumber regime of stable two-dimensional rolls is limited to the neighbourhood of the critical point ($Ra_c = 657; \alpha_c = 2.23$) by the presence of cross-roll and skewed varicose instabilities. The growth rate of the skewed varicose instability vanishes as the Prandtl number approaches infinity. Thus, the stable planforms are different for large (but finite)-Prandtl-number fluids and effectively infinite-Prandtl-number fluids when the boundaries are stress-free. Two-dimensional rolls are virtually always unstable at finite Prandtl number, whereas they remain stable in the limit of infinite Prandtl number well beyond the critical Rayleigh number. Bolton & Busse (1985) have determined the wavenumber limits for stable two-dimensional rolls for $Ra < 2\times10^4$, and their results are reproduced in figure 1. They found that the stability boundaries (defined by the occurrence of high- and low-wavenumber cross-rolls, respectively) do not intersect below $Ra = 2\times10^4$, and unlike the case of Rayleigh–Bénard convection between rigid surfaces, rolls with wavenumbers near the critical value remain stable. Recently, Schnaubelt & Busse (1989) have extended the analysis to high Rayleigh numbers, in an effort to determine if a Rayleigh number limit to stable rolls exists.

Using a Galerkin method (modal expansion), Schnaubelt & Busse found that stability of two-dimensional rolls is extremely sensitive to the truncation level used in the modal expansion. In the region of stable rolls, the growth rate of cross-roll instabilities decreased as the truncation level increased. They concluded that rolls with wavenumbers near three are marginally stable for $Ra < 10^6$ and perhaps even higher. Their extension of the Bolton & Busse curve is shown in figure 1.

Fully three-dimensional numerical simulations of Rayleigh–Bénard convection in large domains are now practical and the literature on this subject is growing rapidly. Most of the published results are for finite-Prandtl-number fluids (Grötzbach 1982; Curry, Herring & Orszag 1984; Clever & Busse 1989). Even for the restricted case of infinite Prandtl number and stress-free boundaries, which is the relevant case for mantle convection, results have been reported recently for both Cartesian (Frick, Busse & Clever 1983; Cserepes, Rabinowicz & Rosenberg-Borot 1988; Houseman 1988) and spherical shell geometries (Baumgardner 1985; Bercovici *et al.* 1989; Glatzmaier 1989; Machetel, Rabinowicz & Bernardet 1986; Zebib, Goyal & Schubert 1985). There has been no comprehensive analysis of planform instabilities in Cartesian geometry. In this paper we demonstrate that it is necessary to use domains with large horizontal dimensions in order to determine the preferred planforms when the flow is fully three-dimensional. The results obtained to date using spherical shell geometries, generally limited to Rayleigh numbers below 10^5, are remarkably consistent in one respect. They indicate that the preferred planform consists of descending sheet-like flow surrounding columnar or broad upwellings, irrespective of the mode of heating, or the presence of compressibility (Bercovici *et al.* 1989). If it is confirmed that this flow structure persists at larger Rayleigh numbers, and is not destroyed by introduction of temperature-dependent rheology, then this result constitutes an important theoretical prediction of the structure of mantle convection on the largest scales. In §5 we show that similar flow structures can occur even in the relatively simple case of base-heated plane layer convection.

2. Planform instabilities

The simplest possible planform of motion in cellular convection, and the one that serves as the basic state in these calculations, is periodic two-dimensional rolls, with a single non-zero component of vorticity along some horizontal direction. These are referred to as *stable rolls* (SR). A *cross-roll* (CR) instability results in the replacement of a set of rolls with unstable wavenumber by an orthogonal set with a stable wavenumber. The final state is again two-dimensional. *Bimodal* (BM) convection is three-dimensional flow consisting of a superposition of two orthogonal sets of rolls. In the classic bimodal instability, as it occurs in Rayleigh–Bénard convection with rigid boundaries, the secondary rolls have smaller amplitude and higher wavenumber than the primary set. *Knot convection* consists of bimodal flow with well-developed orthorhombic ascending and descending plumes. A variation of this flow is bimodal convection with hexagonal knots, due to the presence of oblique sets of disturbance rolls. In this paper, bimodal flows with well-defined vertices are collectively referred to as knot convection, as the term is used by Clever & Busse (1989). Fully three-dimensional periodic cellular flows, in which centres of vertical motion are separated by completely connected regions with opposing vertical motion include *hexagons* (HX) and *rectangles*, with *square cells* (SQ) being a special case of the latter. Two polarities are possible for these planforms, for example up-hexagons (HX+) with rising columns surrounded by sinking sheets, and down-hexagons (HX−) with the directions of motion reversed. A description of these symmetries in terms of normal mode components is given in Malkus & Veronis (1958) and in Busse (1981).

3. Governing equations and method of solution

Conservation of momentum, mass and energy for thermal convection in an infinite-Prandtl-number, Boussinesq fluid layer can be written in dimensionless form as

$$\nabla^2 \boldsymbol{u} = \nabla P - Ra\, T\hat{\boldsymbol{z}}, \tag{1}$$

$$\nabla \cdot \boldsymbol{u} = 0, \tag{2}$$

$$\frac{\partial}{\partial t} T + (\boldsymbol{u} \cdot \nabla)\, T = \nabla^2 T, \tag{3}$$

where $\boldsymbol{u}$ is the fluid velocity, T is temperature, P is pressure with the hydrostatic component removed, $\hat{\boldsymbol{z}}$ is the unit vertical vector, and Ra is the Rayleigh number, given by

$$Ra = \frac{\beta g \Delta T D^3}{\kappa \nu}. \tag{4}$$

Here ΔT is the temperature difference between bottom and top surfaces of the fluid, β is the thermal expansion coefficient, g is acceleration due to gravity, κ is thermal diffusivity, ν is kinematic viscosity and D is the layer depth, all assumed constant. Equations (1)–(3) are made dimensionless using the layer depth D, the thermal diffusion timescale D^2/κ and the applied temperature difference ΔT as units of length, time and temperature, respectively. The pressure scale is $\rho\nu\kappa/D^2$, where ρ is the undisturbed fluid density.

We decompose (1) into scalar equations by expressing the velocity field as the sum of a poloidal and toroidal part, $\boldsymbol{u}_\mathrm{P}$ and $\boldsymbol{u}_\mathrm{T}$, each satisfying incompressibility (2) identically:

$$\boldsymbol{u} = \boldsymbol{u}_\mathrm{P} + \boldsymbol{u}_\mathrm{T} = \nabla \times \nabla \times \hat{\boldsymbol{z}}\psi + \nabla \times \hat{\boldsymbol{z}}\tau. \tag{5}$$

In terms of the scalar potentials ψ and τ the (x, y, z) components of velocity (u, v, w) are:

$$u = \frac{\partial \tau}{\partial y} + \frac{\partial^2 \psi}{\partial x \partial z}, \quad v = -\frac{\partial \tau}{\partial x} + \frac{\partial^2 \psi}{\partial y \partial z}, \quad w = -\left(\frac{\partial^2}{\partial x^2} + \frac{\partial^2}{\partial y^2}\right)\psi. \tag{6a–c}$$

Application of the operators $(\hat{\boldsymbol{z}} \cdot \nabla \times)$ and $(\hat{\boldsymbol{z}} \cdot \nabla \times \nabla \times)$ to (1) and substitution of (5) results in

$$\nabla^2 \tau = 0 \tag{7}$$

and

$$\nabla^4 \psi = Ra\, T. \tag{8}$$

In terms of ψ, τ and T, the boundary conditions are as follows. The horizontal surfaces are assumed to be impermeable, free-slip and isothermal, so that

$$\psi = \frac{\partial^2 \psi}{\partial z^2} = \frac{\partial \tau}{\partial z} = 0, \quad z = 0, 1; \quad T = 1, 0, \quad z = 0, 1. \tag{9a, b}$$

The domain of computation consists of a rectangular box with unit height and with horizontal dimensions X and Y in the x- and y-coordinate directions. All vertical sidewalls are assumed to be impermeable, free-slip and thermally insulating, which results in the conditions

$$\tau = \frac{\partial\psi}{\partial x} = \frac{\partial^3\psi}{\partial x^3} = \frac{\partial T}{\partial x} = 0, \quad x = 0, X, \tag{10a}$$

$$\tau = \frac{\partial\psi}{\partial y} = \frac{\partial^3\psi}{\partial y^3} = \frac{\partial T}{\partial y} = 0, \quad y = 0, Y. \tag{10b}$$

It is immediately seen that the solution to (7) for the toroidal stream function satisfying conditions (9) and (10) is identically zero.

Equations (3) and (8), subject to the boundary conditions given by (9) and (10), are solved numerically using the following scheme. The finite-difference mesh consists of rectangular cells with dimensions $(\Delta x, \Delta y, \Delta z)$. Both the stream function ψ and the velocity components (u, v, w) are evaluated at cell corners, while temperature T is evaluated at cell centres. Time is advanced explicitly, and ψ is determined using temperatures from the preceding time step.

The biharmonic equation (8) is first reduced to a set of Poisson equations

$$\nabla^2\omega = Ra\, T, \quad \nabla^2\psi = \omega \tag{11a, b}$$

with the higher derivative boundary conditions written in terms of ω. Fourier transformation of (11) in the horizontal plane yields

$$\left(\frac{\mathrm{d}^2}{\mathrm{d}z^2} - k^2\right)\hat{\omega} = Ra\,\hat{T}, \quad \left(\frac{\mathrm{d}^2}{\mathrm{d}z^2} - k^2\right)\hat{\psi} = \hat{\omega}, \tag{12a, b}$$

where $k^2 = k_x^2 + k_y^2$ and the carets denote Fourier transforms. The ordinary differential equations (12) are discretized using centred differences, and the resulting tridiagonal matrix equation, including the Fourier transformed boundary conditions (9) and (10), is solved using cyclic reduction (Sweet 1977). Velocity components are then calculated by inverse Fourier transformation of $\hat{\psi}$ and centred-difference approximations of (6).

The temperature equation (3) is advanced in time using an $O(\Delta t^2, \Delta x^4)$ finite-difference scheme. Integration of (3) over a cell volume $\Delta\Omega$, and approximation of the time derivative by a forward difference yield

$$\int\!\!\int\left[\frac{\partial T}{\partial t} + \nabla\cdot(\boldsymbol{u}T - \nabla T)\right]\mathrm{d}\Omega\,\mathrm{d}t \approx (T^{n+1} - T^n)\,\Delta\Omega + \int_l\!\int(\boldsymbol{u}T - \nabla T)^n\cdot\mathrm{d}\boldsymbol{A}_l\,\mathrm{d}t, \tag{13}$$

where n is the time level and $l = 1, 2, 3$ denotes the cell face, whose area is $\boldsymbol{A}_l$. Over each cell face the second term on the right-hand side of (13) is evaluated as

$$\int\!\!\int(\boldsymbol{u}T - \nabla T)\cdot\mathrm{d}\boldsymbol{A}\,\mathrm{d}t \approx \Delta t\int\!\!\int(\boldsymbol{u}T - \nabla T)^n\cdot\mathrm{d}\boldsymbol{A},$$

which is integrated exactly, for example, on the x_3 face as

$$\Delta t\int_0^{\Delta x_1}\!\int_0^{\Delta x_2}\left[u(x_1, x_2)\,T(x_1, x_2) - \frac{\partial T}{\partial x_3}(x_1, x_2)\right]\mathrm{d}x_1, \mathrm{d}x_2, \tag{14}$$

$$\text{where} \quad u(x_1, x_2) = u_1 + (u_2 - u_1)\frac{x_1}{\Delta x_1} + (u_3 - u_1)\frac{x_2}{\Delta x_2} + (u_4 + u_1 - u_2 - u_3)\frac{x_1 x_2}{\Delta x_1\,\Delta x_2}, \tag{15}$$

and u_i is the normal velocity component at the ith corner of the face. A similar expression is used for temperature:

$$T(x_1, x_2) = \bar{T}_1 + (\bar{T}_2 - \bar{T}_1)\frac{x_1}{\Delta x_1} + (\bar{T}_2 - \bar{T}_1)\frac{x_2}{\Delta x_2} + (\bar{T}_4 + \bar{T}_1 - \bar{T}_2 - \bar{T}_3)\frac{x_1 x_2}{\Delta x_1 \Delta x_2}, \tag{16}$$

where $\bar{T}_i$ is the temperature value at the ith corner, found by interpolating the temperature values from the midpoints of adjacent cells.

Forward time differencing in (13) introduces numerical dispersion, as can be seen by considering the truncation error. The Taylor series expansion of the first term on the right-hand side of (13) near time step n is, to first order,

$$\frac{T^{n+1} - T^n}{\Delta t} \approx \left(\frac{\partial T}{\partial t}\right)^n + \tfrac{1}{2}\Delta t \left(\frac{\partial^2 T}{\partial t^2}\right)^n + O(\Delta t^2). \tag{17}$$

Differentiating (3) with respect to t and using (17) yields (Ramshaw & Dukowicz 1979)

$$\frac{T^{n+1} - T^n}{\Delta t} \approx \left(\frac{\partial T}{\partial t}\right)^n + \tfrac{1}{2}\Delta t \nabla \cdot \boldsymbol{F} + O(\Delta t^2), \tag{18}$$

where

$$\boldsymbol{F} = \boldsymbol{u}(\boldsymbol{u} \cdot \nabla T). \tag{19}$$

The differential equation that is being approximated by the difference equation (13) is actually

$$\frac{\partial T}{\partial t} + \nabla \cdot (\boldsymbol{u}T) = \nabla \cdot \nabla T - \tfrac{1}{2}\Delta t \nabla \cdot \boldsymbol{F} \tag{20}$$

with the last term representing the source of numerical dispersion. The amplitude of this dispersion is negative, and therefore destabilizing. Its effect can be removed by adding a term with the opposite sign, so that the difference equation then becomes

$$\frac{T^{n+1} - T^n}{\Delta t} + \nabla \cdot (\boldsymbol{u}T)^n = \nabla \cdot (\nabla T)^n + \nabla \cdot (\boldsymbol{Q} \cdot \nabla T)^n \tag{21}$$

where

$$\boldsymbol{Q} = \tfrac{1}{2}\Delta t \boldsymbol{u}\boldsymbol{u} \tag{22}$$

is the tensor diffusivity required to make (21) an $O(\Delta t^2)$ approximation to the temperature equation.

4. Stability of two-dimensional rolls

We have examined the stability of two-dimensional roll solutions with respect to three-dimensional disturbances for Rayleigh numbers up to 5×10^5 for initial state wavenumbers α_x in the range $1.6 < \alpha_x < 5$, corresponding to cell aspect ratios (cell width/layer depth) in the range $1.96 > X > 0.63$. These calculations were started by projecting a two-dimensional solution onto the three-dimensional grid so that the initial state is uniform in the y-direction. The computational domain imposes basic horizontal wavenumbers $(\alpha_x, \alpha_y) = (\pi/X, \pi/Y)$.

The two-dimensional solutions were obtained by integrating two-dimensional versions of (3) and (8), subject to boundary conditions (9) and (10), forward in time, as described in §3, for a particular Rayleigh number and cell aspect ratio, until a thermally equilibrated flow was obtained. In most cases the equilibrium solution was also a steady state; however, in the cases with largest aspect ratio (smallest basic wavenumber) the two-dimensional flow never reached steady state. Instead, the solution exhibited finite-amplitude oscillations about a mean state, caused by recurring instabilities in the thermal boundary layers. This is a well-known effect in two-dimensional convection calculations with large-aspect-ratio cells (Christensen 1987; Machetel & Yuen 1987). After projection onto the three-dimensional grid, a random temperature perturbation was added at every interior grid point, and the calculations were restarted at the same Rayleigh-number value. Some of the low-Rayleigh-number cases required integration to three or more diffusion time units to reach a steady state. The cases with higher Rayleigh number ($\geqslant 10^5$) generally established stable patterns within one half of a diffusion time unit. All of the cases we discuss in this paper settled into what appear to be highly symmetric states, although this does not guarantee that the solution would remain in such a state indefinitely.

The calculations presented in this section were made with two purposes in mind. First, calculations at low *Ra* ($< 2 \times 10^4$) are used for comparison with the stability theory results of Bolton & Busse (1985) and Schnaubelt & Busse (1989), in order to verify the numerical method. The remainder of the calculations were made to determine the domain of stable rolls as the Rayleigh number is increased beyond 2×10^4.

Figure 1 summarizes the results of the calculations on stability of two-dimensional convection. Numerical experiments are identified by numbers, as in table 1. Filled symbols are used to denote the final states, with circles, diamonds, squares and hexagons referring to roll, bimodal, rectangular and hexagonal planforms respectively. Calculations in which cross-roll instabilities occurred are represented by two circles. Open circles refer to α_x, the initial roll wavenumber in the x-direction. Filled circles refer to α_y, the basic wavenumber of the box in the y-direction. The large circles indicate the final orientation of the roll solution. Thus the domain of stable rolls excludes all polygon symbols and all small open circles, and it includes all large circles. Figure 1 also shows the stability boundaries determined by Bolton & Busse (1985) as solid curves with CR denoting cross-roll instability. Zigzag instabilities are not likely to occur in the limited domains used in these calculations, and as discussed above, the skewed varicose instability is not expected to occur at infinite Prandtl number and therefore are not shown. The lowest solid curve corresponds to onset of convection; the dashed continuations of the cross-roll instability curves represent the approximate limits of stable two-dimensional convection determined by our numerical results. Dotted lines are the side boundaries as determined by Schnaubelt & Busse (1989).

Calculations 1–9 test the stability of small-aspect-ratio, high-wavenumber rolls. In calculations 1–4 and 6, a two-dimensional flow with basic wavenumber $\alpha_x = 4.5$ ($X = 0.7$) was used as the initial condition in a rectangular box with third dimension $Y = 1.41$, corresponding to $\alpha_y = 2.23$, the critical wavenumber at onset of convection. Since instabilities with this wavenumber often are found to have the fastest growth rates in linear stability analyses (Straus 1972; Bolton & Busse 1985), it is reasonable to choose it as the basic periodicity in the third dimension. All of these calculations resulted in cross-roll instabilities, as expected, with the final state consisting of a single steady roll in the (y, z)-plane. Case 1 began from an initial conductive state and evolved into a convective state, with flow in the (y, z)-plane.

Whereas calculations 1–4 and 6 tested flows well outside the cross-roll instability boundaries, calculation 5 was made with $\alpha_x = 4.2$ and $\alpha_y = 3.6$, values just outside and just inside the stability boundary, respectively, as determined by linear analysis.

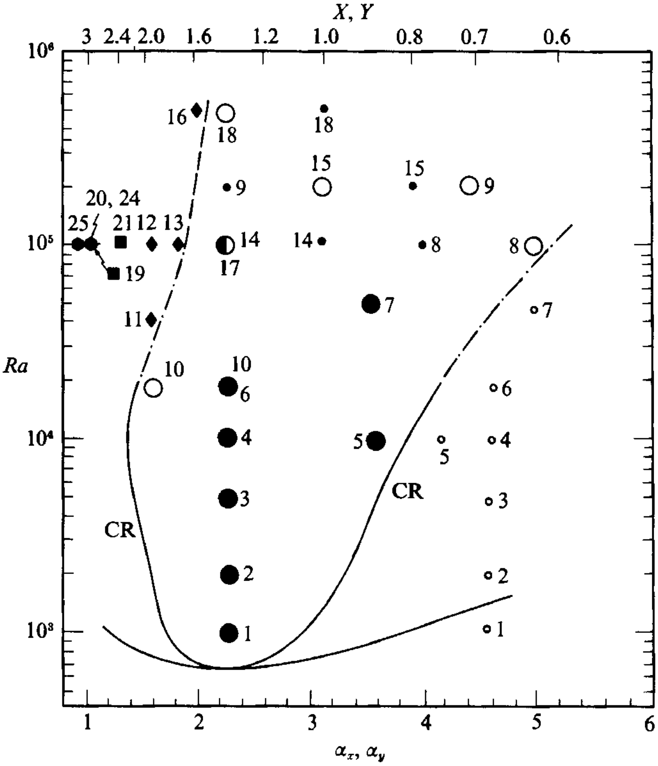

FIGURE 1. Rayleigh number–wavenumber diagram for the stability of two-dimensional rolls in infinite-Prandtl-number thermal convection with free-slip boundaries. Central region corresponds to the domain of stable roll solutions. Solid curves are the stability boundaries as determined by Bolton & Busse (1985) for $Pr = 10^4$. Dotted curves are the extensions determined by Schaubelt & Busse (1989). Symbols denote the final-state planform. Circles denote two-dimensional rolls, diamonds denote bimodal convection, squares and hexagons denote rectangular and hexagonal planforms, respectively. Numbers correspond to the calculations listed in table 1. Calculations resulting in cross-roll (CR) instabilities are denoted by two circles: open circles represent the initial state wavenumber α_x; filled circles represent α_y, the basic wavenumber of the rectangle in the y-direction; large circles denote the final orientation of the roll solution. The field of stable rolls includes all large circles and excludes all three-dimensional solutions and all small open circles. The dashed continuations of the stability boundaries are approximate.

As indicated in figure 1, cross-roll instability occurred, as predicted by theory. This result, along with the result of calculation 10, which used an initial state just within the stability boundary and did not produce cross-roll instability, demonstrates that our numerical method correctly determines stable planform regimes.

Calculations 7–9 were made to extend the high-wavenumber limit of stable rolls to larger Rayleigh numbers. The boundary is best constrained by calculations 7 ($\alpha_x = 5$, $\alpha_y = 3.6$, $Ra = 5 \times 10^4$) and 8 ($\alpha_x = 5$, $\alpha_y = 4$, $Ra = 10^5$) which were unstable and stable, respectively, to cross-roll disturbances. As Schnaubelt & Busse (1989) found, the domain of stable rolls continues to broaden on the high-wavenumber side as the Rayleigh number increases beyond 2×10^4. This is substantiated by the results of calculation 9 ($\alpha_x = 4.4$, $\alpha_y = 2.23$, $Ra = 2 \times 10^5$) in which the initial roll solution remained stable. The domain of stable rolls shows no indication of terminating on the high wavenumber side of figure 1, up to $Ra = 2 \times 10^5$. Because of this behaviour, and because the character of solutions with small initial wavenumbers proved to be more interesting, we did not pursue the high-wavenumber solutions any further.

Case no.	*Ra*	$\alpha_x(X)$	$\alpha_y(Y)$	Grid (X, Y, Z)	I.C.	Result	*KE*/vol	ave *Nu*
1	10^3	4.5 (0.7)	2.23 (1.41)	12, 22, 16	CD	CR	23.75	1.718
2	2×10^3	4.5 (0.7)	2.23 (1.41)	12, 22, 16	2D	CR	110.16	2.674
3	5×10^3	4.5 (0.7)	2.23 (1.41)	12, 22, 16	2D	CR	437.70	3.743
4	10^4	4.5 (0.7)	2.23 (1.41)	12, 22, 16	2D	CR	1085.2	4.639
5	10^4	4.19 (0.75)	3.59 (0.875)	12, 14, 16	2D	CR	750.1	4.696
6	2×10^4	4.5 (0.7)	2.23 (1.41)	12, 22, 16	2D	CR	2597.2	5.655
7	5×10^4	5.03 (0.625)	3.59 (0.875)	15, 21, 24	2D	CR	6696.2	8.276
8	10^5	5.03 (0.625)	4 (0.781)	20, 25, 32	2D	SR	1.077×10^4	9.859
9	2×10^5	4.37 (0.72)	2.23 (1.41)	23, 45, 32	2D	SR	3.285×10^4	12.88
10	2×10^4	1.6 (1.96)	2.23 (1.41)	32, 23, 16	2D	SR	2202.8	6.103
11	4×10^4	1.6 (1.96)	2.23 (1.41)	48, 34, 24	2D	BM	6501.6	7.100
12	10^5	1.6 (1.96)	2.23 (1.41)	48, 34, 24	2D	BM	1.927×10^4	8.883*
13	10^5	1.85 (1.7)	3.14 (1)	40, 24, 24	2D	BM	1.770×10^4	9.244
14	10^5	2.23 (1.414)	3.14 (1)	45, 32, 32	2D	SR	1.954×10^4	9.740
15	2×10^5	3.14 (1)	3.9 (0.8)	36, 28, 36	2D	SR	4.474×10^4	13.11
16	5×10^5	1.93 (1.625)	3.14 (1)	78, 48, 48	2D	BM	1.284×10^5	15.83*
17	10^5	2.23 (1.41)	2.23 (1.41)	34, 34, 24	2D	SR	1.907×10^4	9.299
18	5×10^5	2.23 (1.41)	3.14 (1)	45, 32, 32	2D	SR	1.43×10^5	15.96
19	10^5	1.05 (3)	1.05 (3)	72, 72, 24	2D	SQ$^+$	1.936×10^4	9.307
20	10^5	1.05 (3)	1.05 (3)	72, 72, 24	RN	HX$^+$	1.911×10^4	9.589
21	10^5	1.31 (2.4)	1.31 (2.4)	58, 58, 24	RN	SQ$^-$	1.904×10^4	8.711*
22	10^5	2.23 (1.41)	3.14 (1)	34, 24, 24	2D	SR	1.943×10^4	9.718
23	2×10^5	3.14 (1)	3.9 (0.8)	24, 19, 24	2D	SR	4.426×10^4	13.04
24	2×10^5	1.05 (3)	1.05 (3)	72, 72, 24	HX	HX$^-$	1.91×10^4	9.560
25	10^5	0.9 (3.5)	0.9 (3.5)	84, 84, 24	HX+	HX+	1.88×10^4	9.216*

TABLE 1. List of computational parameters. CD = conduction; CR = cross-roll; 2D = two-dimensional roll; SR = stable roll; BM = bimodal convection; SQ = rectangular or square cell; HX = hexagonal cell; +, − = up, down centre; RN = random temperatures; * = time average for *Nu* and *KE*

In an effort to extend the stable roll regime at intermediate wavenumbers to higher Rayleigh numbers, calculations were made with parameter values (α_x, α_y, Ra) of (2.23, 3.14, 10^5), (3.14, 3.9, 2×10^5), (2.23, 2.23, 10^5) and (2.23, 3.14, 5×10^5), with the results indicated in figure 1 by numbers 14, 15, 17 and 18, respectively. As was the case for high-wavenumber initial states, the region of stable rolls with intermediate wavenumbers definitely extends to at least $Ra = 5\times10^5$. All of the solutions with intermediate- and high-wavenumber initial states eventually settled into steady two-dimensional flows.

The results are very different for flows with initially small wavenumbers (large aspect ratios), representing the left edge of the stable roll field in figure 1. For Rayleigh numbers equal to or less than 2×10^4, the behaviour is similar to the high-wavenumber domain, as indicated by calculation 10 made just within the cross-roll instability boundary. However, at larger Rayleigh-number values, the initial two-dimensional state is no longer steady, as pointed out earlier, and there appears to be an association between the onset of time dependence in flow restricted to two dimensions and the appearance of three-dimensional flow, when that restriction is relaxed. This can be seen in the behaviour of calculations 11–13 and 16 (figure 1), all of which began as time-dependent, initially two-dimensional flows. In all four cases, instability set in as a cross-roll disturbance, and the final state is three-dimensional bimodal convection.

The change in planform with increasing distance from the boundary for stable rolls is shown in figures 2, 3 (plate 1), 4 and 5, which illustrate the bimodal states found in calculations 11–13. Calculation 13, with parameter values (1.85, 3.14, 10^5) is evidently very close to the stable roll boundary. As shown in figures 2 and 3 (*a*), the steady state is bimodal convection, with the dominant initial roll supplemented by a weaker cross-roll with wavenumber 3.14 in the y-direction. Although calculation 11 (1.6, 2.23, 4×10^4) has a lower Rayleigh number than calculation 13, it is farther into the three-dimensional regime. Figures 3 (*b*) and 4 show that the stable flow is again bimodal, but in this case the secondary mode ($\alpha = 4.45$) is nearly as large as the primary one. The rising and descending flows occur in well-defined knots, which have a basic orthorhombic symmetry. The planform is similar to ones computed by Clever & Busse (1989) for a fluid with a Prandtl number of seven. As the wavenumber of the initial flow is decreased and the flow departs farther from the region of stable rolls, additional modes of motion appear in the final steady state. Figure 5 shows the final state for calculation 12, with parameter values (1.6, 2.23, 10^5), representing an increase in Rayleigh number from calculation 11 by a factor 2.5. In this case, the final state is again primarily bimodal, but there is a perceptible contribution to the vertical velocity and temperature fields from oblique modes (modes with wave vectors oblique to the x- and y-axes), which results in hexagonal symmetry for the primary rising and sinking knots. These modes appear in the isothermal surfaces as oblique 'thermal ridges' in the top and bottom boundary layers, connected to the primary knots. The secondary or weaker knots retain the orthorhombic symmetry found in the flows closer to the stability boundary.

As a check on the effect of mesh refinement, we recomputed cases 11, 14 and 15 using coarser zoning. Cases 14 and 15 were recalculated using $34 \times 24 \times 24$ and $24 \times 19 \times 24$ grids, respectively. The results are given in table 1 as cases 22 and 23. Kinetic energy for the coarsely zoned calculations is typically 1 % lower than for the more finely zoned calculations, whereas the Nusselt numbers are only about 0.2 % lower. In both cases, the final steady-state temperature and velocity patterns are virtually identical. Case 11 was also repeated with coarser zoning (32, 23, 16) in order to determine how reduced resolution affects the transition to three-dimensional convection (bimodal pattern, in this case). In calculation 11, the initial roll broke down to a bimodal pattern within 1.0 time units, which continued to evolve until about $t = 1.35$, when it settled into its final, steady bimodal pattern. In the more coarsely zoned calculation, the roll pattern began to break down at about the same time, but the development of the final steady bimodal pattern was slower. Oscillations in the position of the central knot continued well beyond $t = 1.5$. The steady state was approached through gradual attenuation of these oscillations.

All of the final bimodal solutions for $Ra \leqslant 10^5$ appear to be steady states. In addition, all of these were obtained from two-dimensional solutions that were inherently time dependent. This suggests a relationship between the onset of time dependence in convection restricted to two dimensions and the occurrence of three-dimensional convection, when that restriction is relaxed. Three-dimensional convection remains steady at Rayleigh numbers for which restricted two-dimensional convection is time dependent.

The onset of time dependence in bimodal convection occurs somewhere within the interval $10^5 \leqslant Ra < 5 \times 10^5$. Bimodal convection is time dependent at $Ra = 5 \times 10^5$, as indicated by the results from case 16 $(\alpha_x, \alpha_y, Ra) = (1.93, 3.14, 5 \times 10^5)$. The time series of kinetic energy for this case is shown in figure 6 and the temperature structure at $t = 0.44$ and 0.45 is shown in figures 3 (*c*) and 3 (*d*). While the

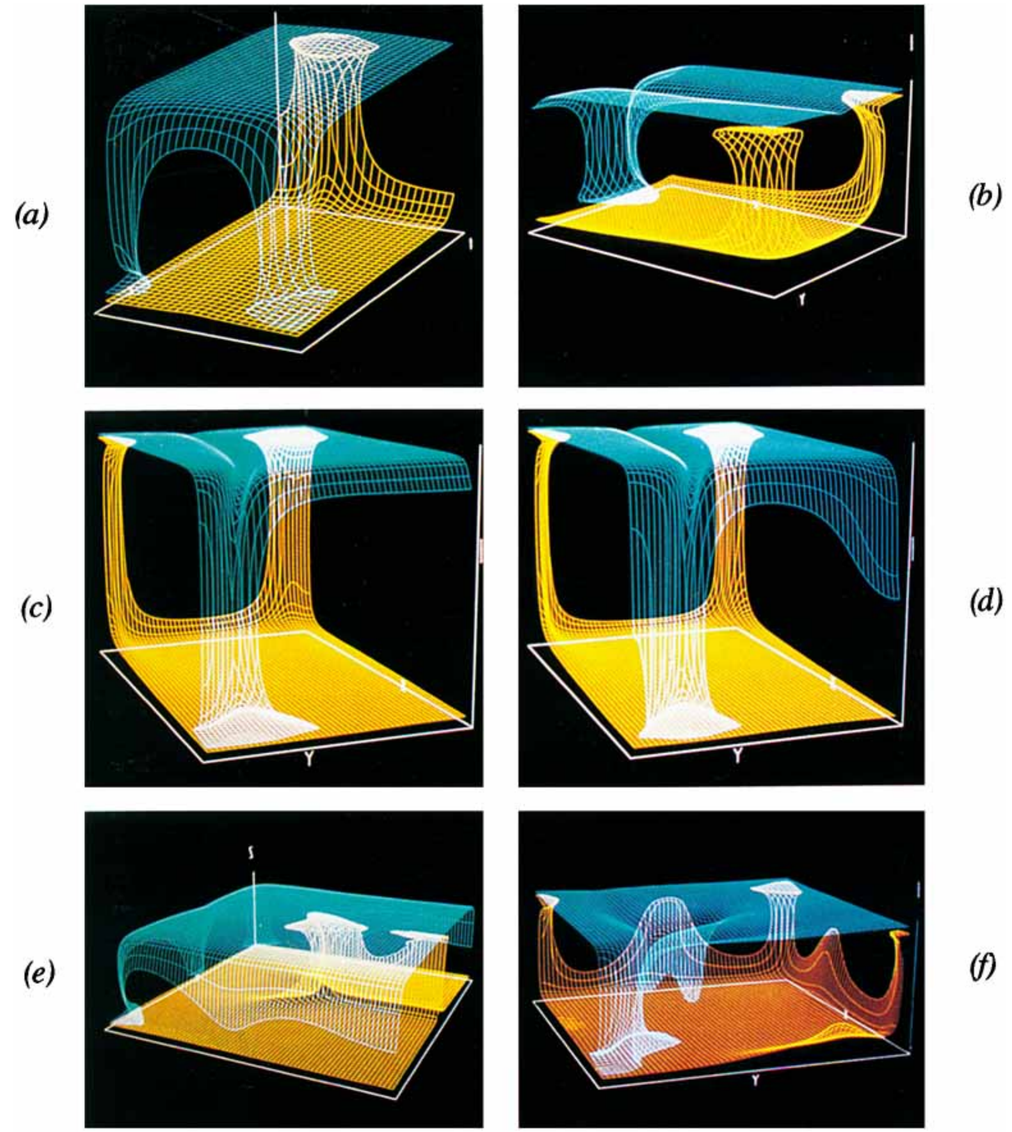

FIGURE 3 (*a*). Constant-temperature surfaces in steady bimodal convection for $\alpha_x=1.85$, $\alpha_y=3.14$ ($X=1.7$, $Y=1.0$), $Ra=10^5$ (calculation 13). The region shown corresponds to the lower right quadrant of the planform shown in figure 2. Shown are isothermal surfaces for $T=0.25$ and 0.75. (*b*) Constant-temperature surfaces in steady bimodal convection for $\alpha_x=1.6$, $\alpha_y=2.23$ ($X=1.96$, $Y=1.41$) and $Ra=4\times10^4$ (calculation 11). The region shown corresponds to the lower left quadrant of the planform shown in figure 4. Shown are isothermal surfaces for $T=0.25$ and 0.75. (*c,d*) Constant-temperature surfaces in unsteady bimodal convection for $\alpha_x=1.93$, $\alpha_y=3.14$ ($X=1.625$, $Y=1$) and $Ra=5\times10^5$ at (*c*) $t=0.44$ and (*d*) $t=0.45$, started from a two-dimensional roll initial condition (calculation 16). Shown are isothermal surfaces for $T=0.25$ and 0.75. (*e*) Constant-temperature surfaces in three-dimensional rectangular cell convection for $\alpha_x=\alpha_y=1.05(X=Y=3)$, $Ra=10^5$ at $t=0.6$, started from an initial two-dimensional solution. Isothermal surfaces are $T=0.25$ and 0.75. Region shown corresponds to upper half of figure 8 planform. (*f*) Constant-temperature surfaces in three-dimensional square cell convection for $\alpha_x=\alpha_y=1.31$ ($X=Y=2.4$), $Ra=10^5$. Region shown corresponds to upper right quadrant of the planform shown in figure 10. Isothermal surfaces are $T=0.25$ and 0.75.

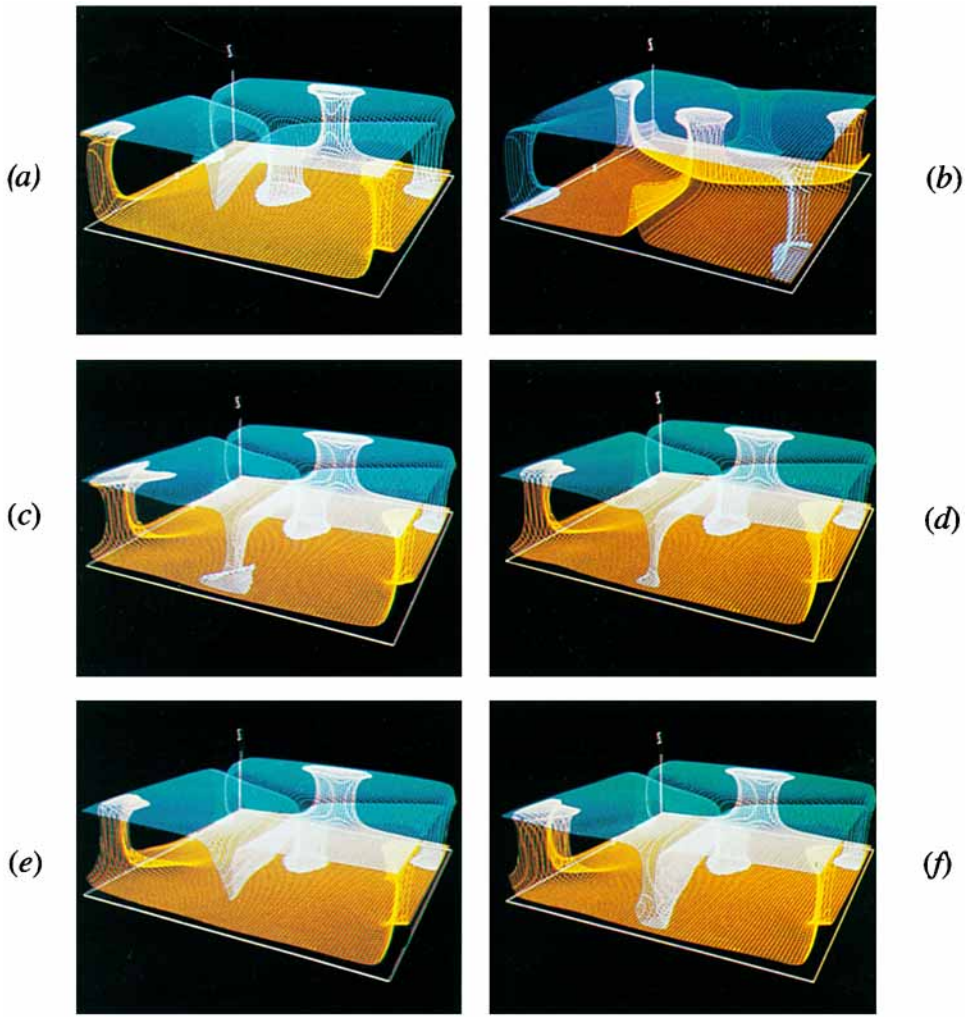

FIGURE 7. (*a*, *b*) Constant-temperature surfaces in hexagonal cell convection for $\alpha_x=\alpha_y=1.05$ ($X=Y=3$), $Ra=10^5$: (*a*) up-hexagon solution (corresponds to lower half of figure 9); (*b*) down-hexagon solution. Isothermal surfaces are $T=0.25$ and 0.75. (*c*–*f*). Constant-temperature surfaces in time-dependent hexagonal cell convection for $\alpha_x=\alpha_y=1.114$ ($X=Y=3.5$) through one period of oscillation at (*c*) $t=0.5260$; (*d*) 0.5277; (*e*) 0.5294; and (*f*) 0.5311.

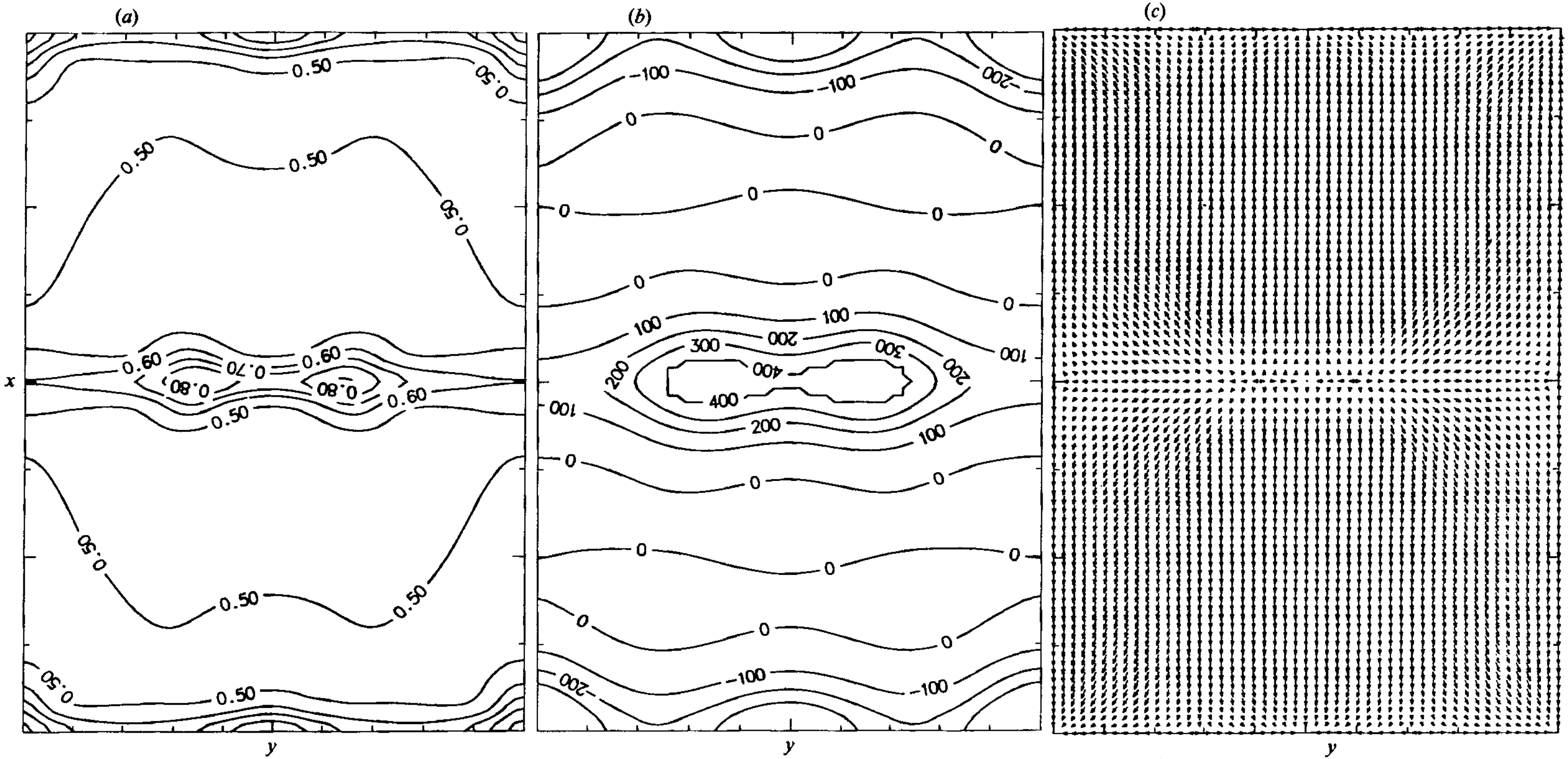

Figure 2. Steady bimodal convection for $\alpha_x = 1.85$, $\alpha_y = 3.14$ ($X = 1.7$, $Y = 1.0$) and $Ra = 10^5$ at $t = 2.05$, starting from an initially two-dimensional solution (calculation 13). (*a*) Midplane ($z = 0.5$) contours of temperature, (*b*) vertical velocity, and (*c*) the pattern of upper surface ($z = 1$) horizontal velocity. This image consists of two reflections of the computational domain, one across the ($x = 1.7$)-plane, the other across the ($y = 1$)-plane.

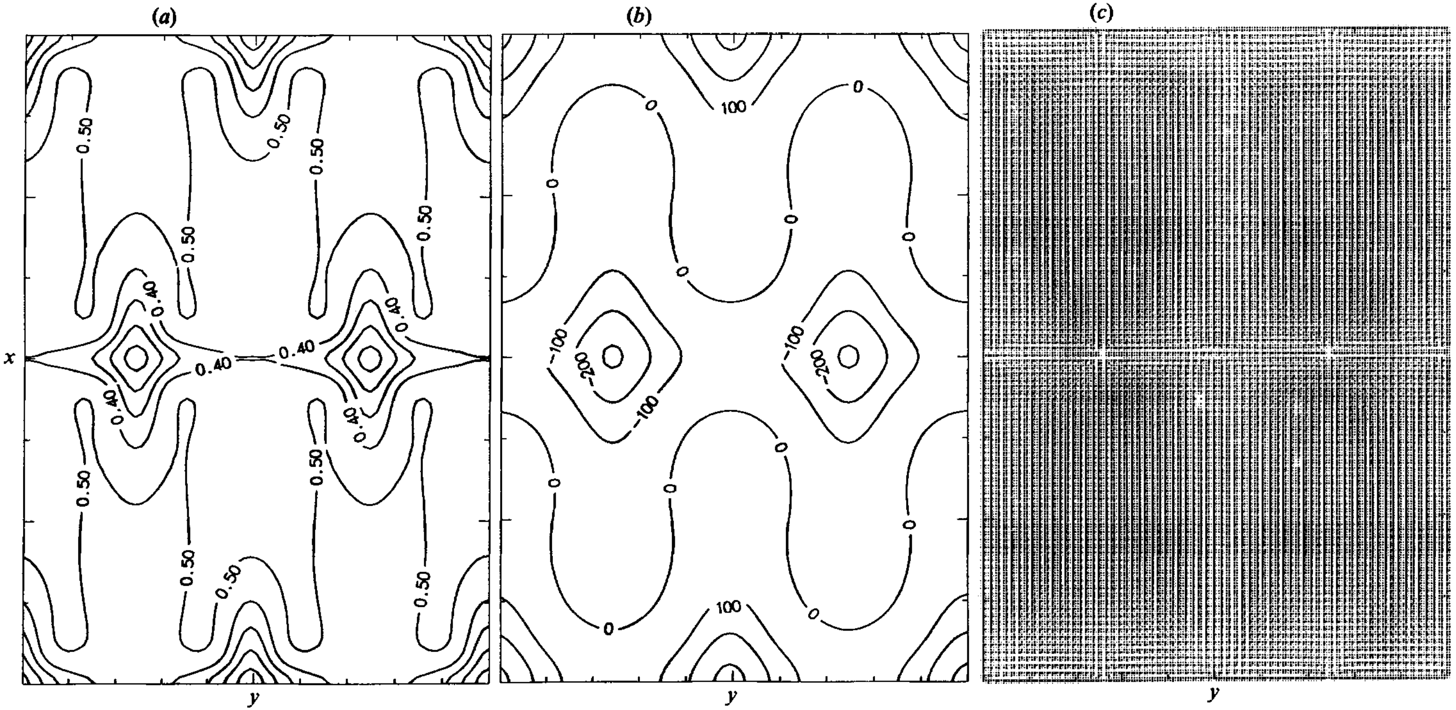

FIGURE 4. Steady bimodal convection for $\alpha_x = 1.6$, $\alpha_y = 2.23$ ($X = 1.96$, $Y = 1.41$) and $Ra = 4 \times 10^4$ at $t = 2.34$, starting from a two-dimensional initial condition (calculation 11). (*a*) Midplane ($z = 0.5$) contours of temperature, (*b*) vertical velocity, and (*c*) the pattern of upper surface ($z = 1$) horizontal velocity. Reflection planes are $y = 1.41$ and $x = 1.96$.

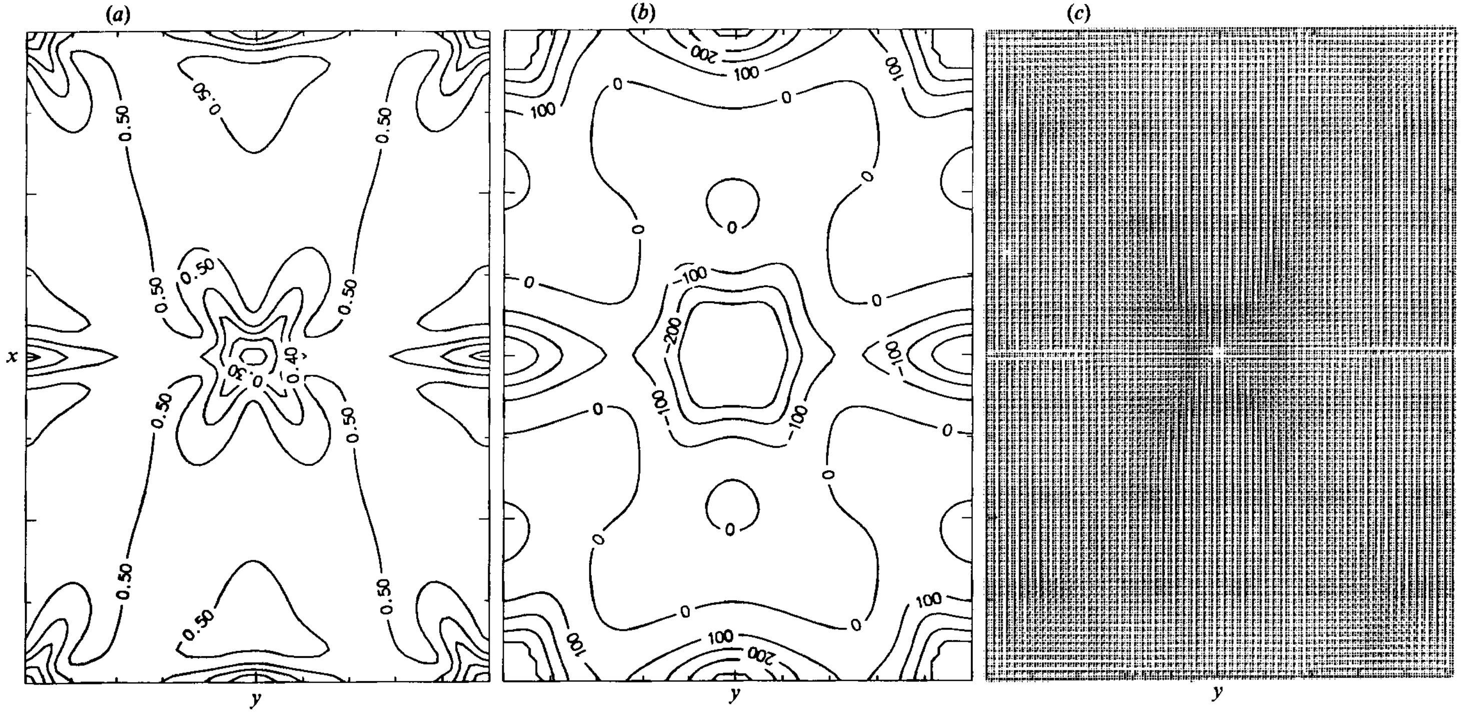

FIGURE 5. Steady bimodal convection with hexagonal primary vertices and orthorhombic secondary vertices for $\alpha_x = 1.6$, $\alpha_y = 2.23$ ($X = 1.96$, $Y = 1.41$), $Ra = 10^5$ at $t = 1.53$ (calculation 12), starting from an initial two-dimensional solution. (*a*) Midplane ($z = 0.5$) contours of temperature, (*b*) vertical velocity, and (*c*) the pattern of upper surface ($z = 1$) horizontal velocity. Reflection planes are $x = 1.96$ and $y = 1.41$.

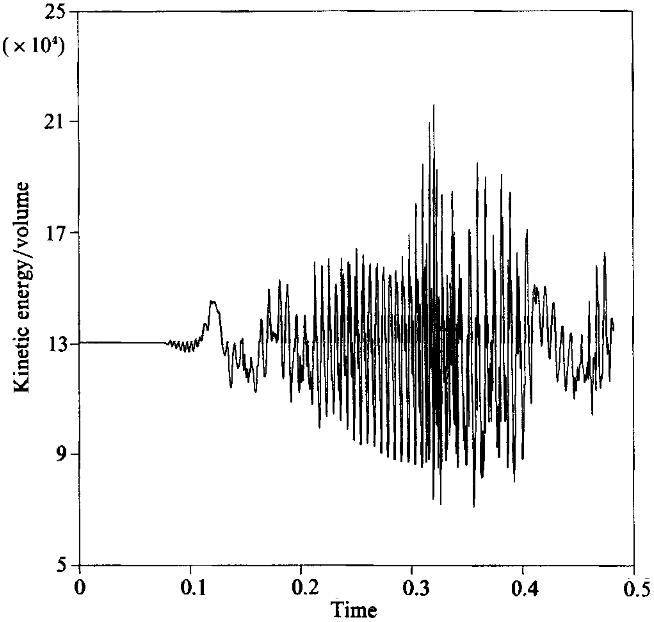

FIGURE 6. Time series of average kinetic energy in time-dependent bimodal convection from calculation 16.

temperature structure is clearly bimodal, it differs from the steady states obtained closer to the stability boundary because of an incipient descending plume, a thermal ridge, which is evident along the z-axis in the $T = 0.25$ isothermal surface (figure 3*c*,*d*). This perturbation, which might represent a pattern-breaking disturbance, is nearly periodic in time although its strength varies from one period to the next. Less noticeable are smaller fluctuations in the three established plumes. These are due to small perturbations in the thermal boundary layers being swept into the plumes by the large-scale flow. Although we cannot verify that the fluctuation is not simply a long transient, there are differences between this case and the steady bimodal flows, which lead us to expect that this solution is truly time dependent. In the cases where steady states were found, the initial three-dimensional patterns were not symmetric, but the symmetry increased with time through a sequence of adjustments, which led to a final symmetric planform. In contrast, case 16 does not show a drift towards a more symmetric planform. Upwellings are twice as numerous as downwellings, and the incipient downwelling plume never becomes fully established. This behaviour is similar to the mechanism for time dependence identified in finite-Prandtl-number convection by Clever & Busse (1989).

5. Three-dimensional convection in large-aspect-ratio rectangular boxes

The flows described in the previous section were computed in rectangular boxes in which the largest horizontal dimension is less than twice the layer depth. This confinement substantially restricts the types of flow that can occur. It is therefore important to determine if different final planforms result when the lateral dimensions of the domain are increased.

In order to address the effects of increased aspect ratio, we have made five additional calculations at $Ra = 10^5$. Three of these were made in a rectangular box

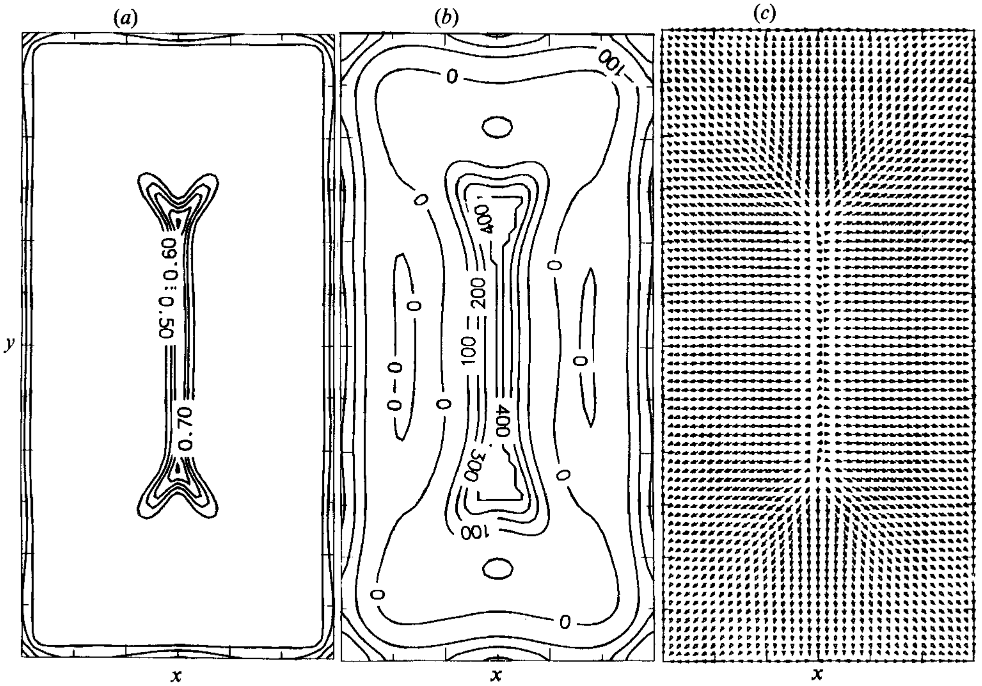

FIGURE 8. Three-dimensional rectangular cell convection for $\alpha_x = \alpha_y = 1.05$ ($X = Y = 3$), $Ra = 10^5$ at $t = 0.6$, started from an initial two-dimensional solution. (*a*) Midplane ($z = 0.5$) contours of temperature, (*b*) vertical velocity, and (*c*) the pattern of upper surface ($z = 1$) horizontal velocity. Reflection plane is $y = 3.0$.

with horizontal dimensions $X = Y = 3$, one with $X = Y = 2.4$ and one with $X = Y = 3.5$. Calculation 19 listed in table 1 had as initial conditions a two-dimensional flow with aspect ratio 3. It therefore represents an extreme case of the stability calculations presented in the previous section. For comparison, calculation 20 was made at the same Rayleigh number and in the same domain as 19, but starting from purely random initial conditions, that is, without a structured temperature field present. Calculation 21 was also started with random temperature conditions in a $2.4 \times 2.4 \times 1$ rectangle. Calculation 24 was made to test the symmetry properties of the hexagonal solution found in calculation 20, and calculation 25 was made to determine if hexagons can persist in very large boxes. Results of these calculations are shown in figures 3, 7 (plate 2) and 8–13. Midplane velocity and temperature fields at $t = 0.6$ for the initially two-dimensional flow in the $3 \times 3 \times 1$ box (calculation 19) are shown in figure 8. Figure 3(*e*) shows the structure of selected isothermal surfaces at the same time. The flow has nearly reached steady state, with kinetic energy fluctuations less than 1% of the mean value. At $t = 0.6$ the flow has settled into a rectangular planform, with ascending motion in the centre and descending flow along the four cell walls (an up-rectangle). The dominant mode consists of aspect ratio 1.5 rolls aligned along the y-direction.

Quite different results were obtained when the calculation was repeated using random initial temperature conditions. Midplane velocity and temperature sections at $t = 0.5$ are shown in figure 9. Figure 7(*a*) shows the structure of selected isothermal surfaces at the same time. In this case the flow settled into a hexagonal planform by $t = 0.03$, and the kinetic energy becomes nearly steady by $t = 0.2$. Very small fluctuations persist to $t = 0.5$, but these do not affect the basic flow symmetry. As

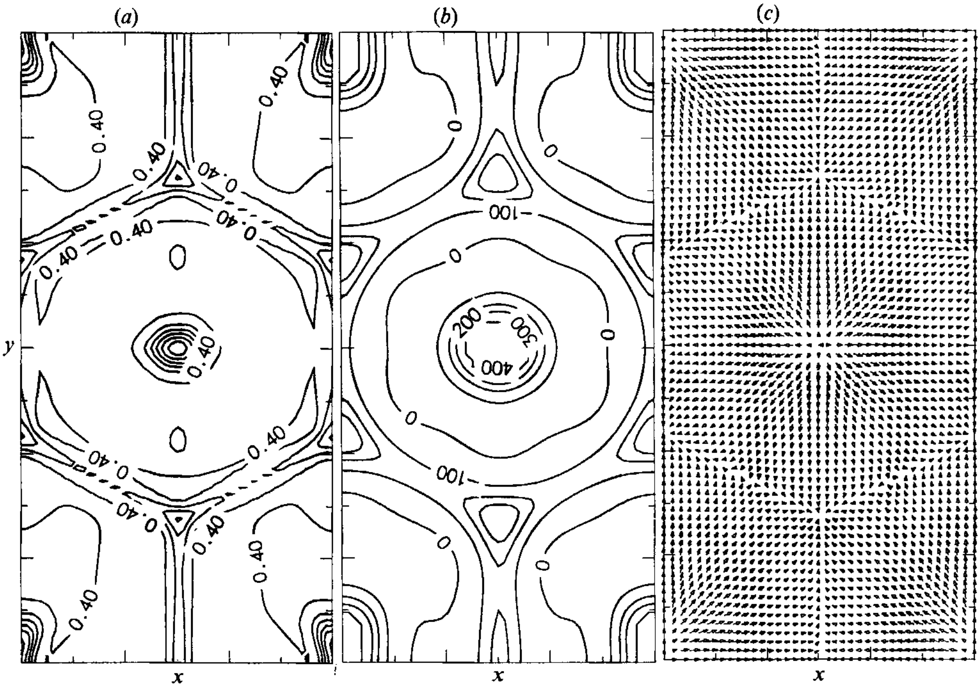

FIGURE 9. Three-dimensional hexagonal cell convection for $\alpha_x = \alpha_y = 1.05$ ($X = Y = 3$), $Ra = 10^5$ at $t = 0.5$, started from random temperature initial conditions (calculation 20). (*a*) Midplane ($z = 0.5$) temperature contours, (*b*) vertical velocity contours, and (*c*) upper surface ($z = 1$) horizontal velocity pattern. Reflection plane is $y = 3.0$.

shown in figures 7 (*a*) and 9, the planform is an up-hexagon, with fully connected descending sheets intersecting at angles $\frac{2}{3}\pi$, surrounding a columnar upwelling. The existence of hexagonal cell solutions was anticipated by the results of the roll stability analysis discussed in the preceding section, in which elongated rolls evolved to bimodal convection with hexagonal knots.

To our knowledge, this is the first demonstration that hexagonal symmetries occur in symmetric base-heated Rayleigh–Bénard convection. It is well established that hexagonal planforms occur just above the critical Rayleigh number when variable fluid properties are present, such as temperature-dependent viscosity (Palm 1960; Busse 1967*b*; Oliver & Booker 1983; White 1988). We have already mentioned the results from spherical-shell convection calculations, which show a preference for flow with descending sheets surrounding rising columns. However, none of the symmetry-destroying effects produced by sphericity, variable properties or internal heat production are present in these calculations, and yet it appears that hexagonal cells are either stable planforms, or are so weakly unstable that the breakdown to rectangular planforms occurs too slowly to appear in our numerical calculations. It is only by coincidence that calculations 19 and 20 resulted in cells with the same polarity. Since the horizontal midplane is a symmetry plane for steady states, there is no preference for either ascending or descending centres. In order to demonstrate this fact, we inverted calculation 20 and used it as the condition for case 24. The result is a down-hexagon, shown in figure 7 (*b*).

The results from the $3 \times 3 \times 1$ box calculations demonstrate the preference for steady three-dimensional cellular planforms with this aspect ratio at $Ra = 10^5$, but

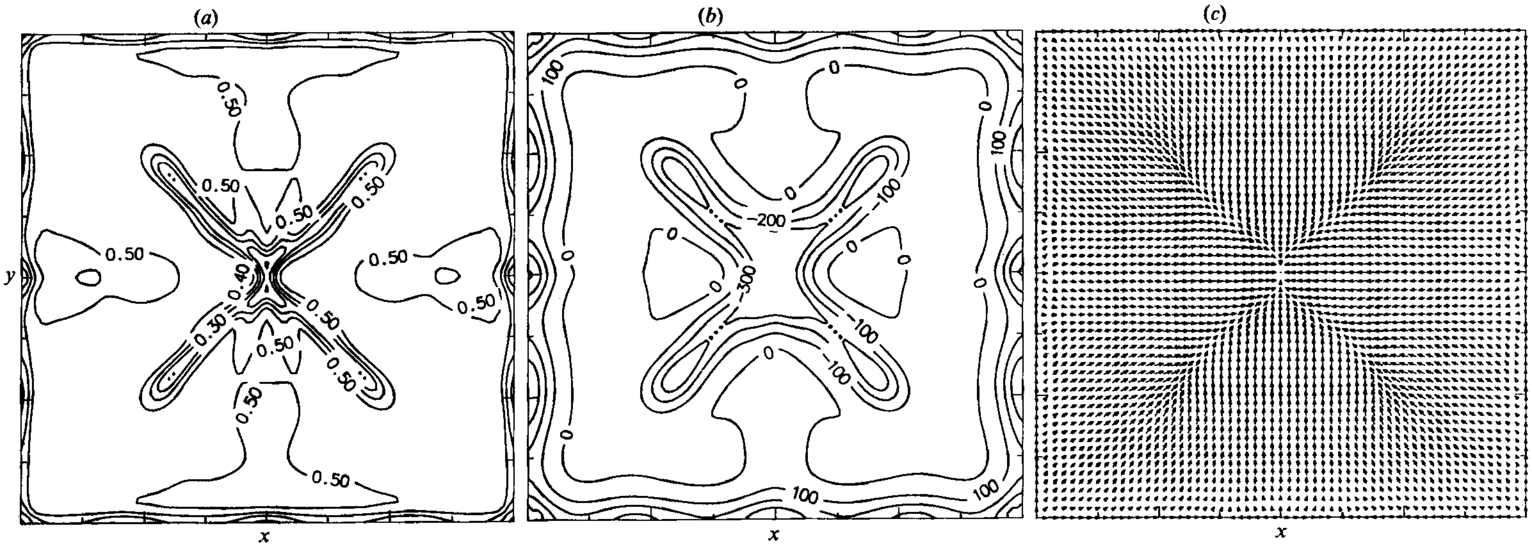

FIGURE 10. Three-dimensional square cell convection for $\alpha_x = \alpha_y = 1.31$ ($X = Y = 2.4$), $Ra = 10^5$ at $t = 0.5$, started from random temperature initial conditions (calculation 21). (*a*) Midplane ($z = 0.5$) temperature contours, (*b*) vertical velocity contours and (*c*) upper surface ($z = 1$) horizontal velocity pattern. Reflection planes are $x = 2.4$ and $y = 2.4$.

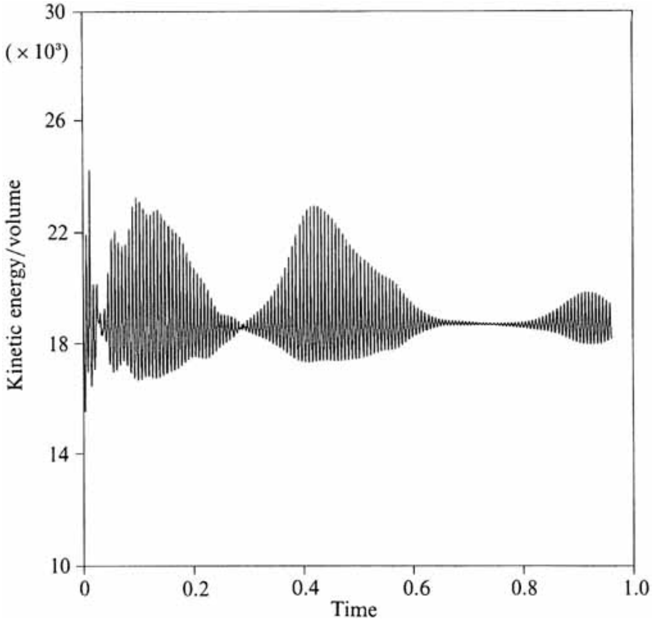

FIGURE 11. Time series of average kinetic energy for time-dependent hexagonal cell convection at $Ra = 10^5$ for $\alpha_x = \alpha_y = 0.9$ ($X = Y = 3.5$).

they do not establish the preferred planform. Indeed, it appears that differences in initial conditions are important in planform selection. In order to provide some additional data on planform preference, we have repeated the random initial temperature condition of calculation 20 in a smaller rectangular box, with dimensions $2.4 \times 2.4 \times 1$ (computational parameters are given in table 1, calculation 21). The planform at $t = 0.5$ is shown in figure 10. The shapes of selected isothermal surfaces are shown in figure 3 (*f*). This calculation produced a down-square planform which appears to be stable, although it does not reach steady state. The kinetic energy continues to fluctuate with $\pm 5\%$ variation about its mean value. These fluctuations appear most conspicuously as variations in the strengths of ascending flow vertices at the midpoints of the cell boundaries, and as variations in the pattern of thermal ridges connected to the central downwelling. The down-square pattern obtained in this case demonstrates again that both up- and down-cellular flows are realizable and it also suggests that rectangular planforms may be preferred over hexagons when the aspect ratio is less than three.

Whereas square cell or bimodal planforms were obtained in small-aspect-ratio boxes, hexagonal planforms are clearly stable in larger domains at $Ra = 10^5$, as indicated by the results of calculation 25. This case was initialized by expanding the hexagonal solution from case 20 to fit a $3.5 \times 3.5 \times 1$ box. The hexagonal planform persisted, but unlike the solution in the $3 \times 3 \times 1$ box it was unsteady, as shown by the kinetic energy time series in figure 11 and the sequence of isothermal surfaces shown in figure 7 (*c*–*f*). Two types of perturbations are present – travelling thermal ridge disturbances in the upper and lower thermal boundary layers and incipient descending plumes which periodically form at specific locations and threaten to alter the basic flow pattern but never succeed. The sequence in figure 7 (*c*–*f*) shows plume development through one cycle, lasting 0.0068 time units. In figure 7 (*c*) the variable plume is fully extended, in 7 (*d*) it has weakened and the kinetic energy of the flow is near its minimum, and in 7 (*e*) a new plume is developing and the kinetic energy

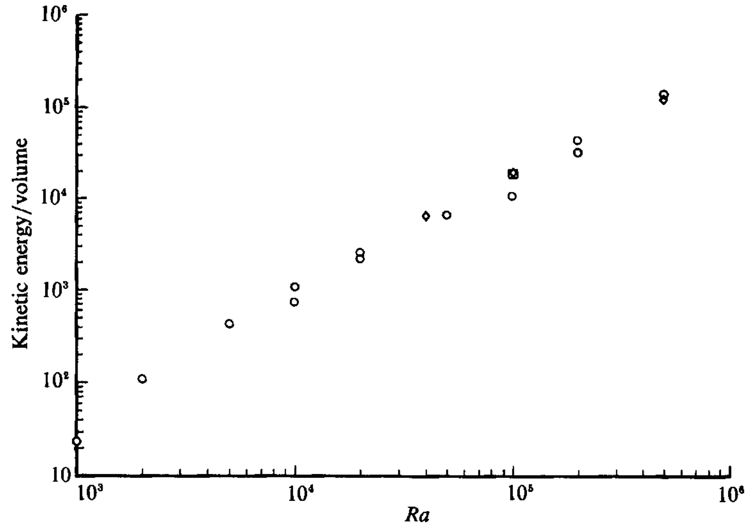

FIGURE 12. Dimensionless kinetic energy density versus Rayleigh number for all calculations. Final planforms are denoted by circles (rolls), diamonds (bimodal convection) and squares (rectangular cells).

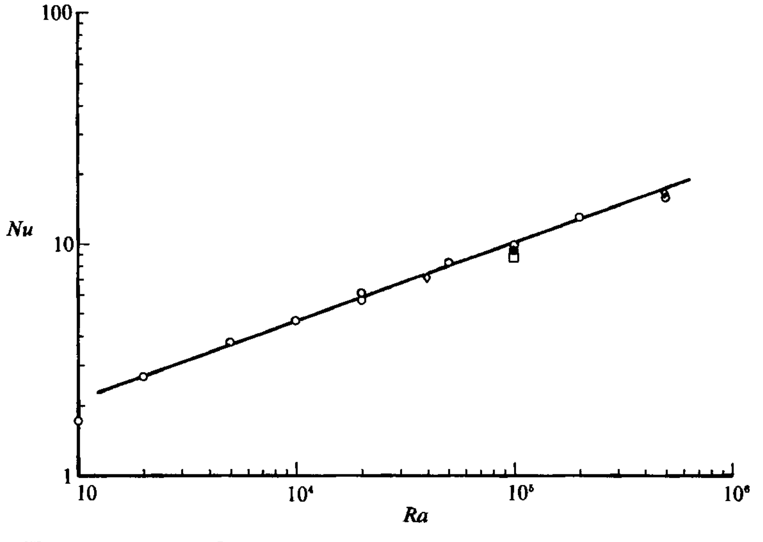

FIGURE 13. Volume-averaged Nusselt number versus Rayleigh number for all calculations. The symbols refer to final state planforms as in figure 12. The heat transfer law $Nu = 0.268Ra^{0.319}$ obtained for $\alpha_x = 3.14$ ($X = 1$) rolls by Schubert & Anderson (1985) is shown for comparison.

is near its maximum. Those time intervals with large kinetic energy fluctuations in figure 11 exhibit this behaviour, while during the quiet intervals the incipient plume is better established and less variable. Only one plume in the box is so variable; the other plumes fluctuate only slightly. The flow appears to be seeking a smaller hexagonal planform but is unable to make the transition.

The dimensionless kinetic energy density and average Nusselt number *Nu* are given for each calculation in table 1. They are plotted against the Rayleigh number in figures 12 and 13. Planform variations in Nusselt number at constant Rayleigh number do not exceed 10%. Among the various planforms, stable roll solutions tend to have the largest Nusselt-number values at a given *Ra*. Figure 13 shows the fit of all calculations to the power law

$$Nu = 0.268Ra^{0.319} \tag{23}$$

obtained for two-dimensional rolls with $\alpha_x = 3.14$ ($X = 1$) by Schubert & Anderson (1985). The deviation from (23) is due to planform variations and to the sensitivity of heat transfer to aspect ratio among the roll solutions. Nevertheless, this comparison indicates that the heat transfer law (23), derived from roll solutions, is a reasonably good zeroth-order predictor of heat transfer in fully three-dimensional convection.

Planform variations in kinetic energy at constant Rayleigh number are greater. For example, at $Ra = 10^5$, the kinetic energy of a stable roll (solution 8) and the fully three-dimensional planforms differ by 90%. In addition, the kinetic energy of stable rolls does not differ systematically from the kinetic energy of the three-dimensional patterns. Indeed, there appears to be little or no relationship between the planform-dependence of kinetic energy and the planform-dependence of Nusselt number.

6. Conclusions

Three-dimensional, time-dependent finite-difference calculations of thermal convection in an infinite-Prandtl-number fluid layer with isothermal and free-slip horizontal boundaries show that steady two-dimensional rolls remain stable for Rayleigh numbers as large as 5×10^5, when the aspect ratio (cell width to depth ratio) is 1.41 or less. Rolls with larger aspect ratios are unstable to three-dimensional disturbances at Rayleigh-number values above approximately 4×10^4. Calculations made in small rectangular domains (with horizontal dimensions less than twice the layer depth) show that time-dependent two-dimensional large-aspect-ratio rolls are unstable and evolve into bimodal convection. In some cases, steady three-dimensional convection is dominantly bimodal but with alternating rows of orthorhombic and hexagonal symmetric knots. Time dependence occurs in bimodal convection at $Ra = 5 \times 10^5$. Calculations in larger aspect ratio domains produce cellular, fully three-dimensional planforms. Steady hexagonal cells evolved from random temperature initial conditions in a $3 \times 3 \times 1$ rectangular domain at $Ra = 10^5$, whereas rectangular cells resulted when the same simulation was initialized with a two-dimensional roll. A square-cell planform was obtained at $Ra = 10^5$ from random initial temperature conditions in a $2.4 \times 2.4 \times 1$ rectangular domain. A hexagonal cell solution at $Ra = 10^5$ in a $3.5 \times 3.5 \times 1$ box exhibits oscillations in kinetic energy and Nusselt number due to the combination of recurring thermal boundary-layer instabilities and incipient plumes. Our results indicate that bimodal, hexagonal and rectangular planforms are all realizable at high Rayleigh numbers, depending on the initial conditions and the area of the rectangular box. The sensitivity of Nusselt number to planform variations is weak. The power law expression $Nu = 0.268Ra^{0.319}$ obtained for aspect-ratio one rolls fits the heat transfer in all of our calculations to within ±5%.

These calculations have been made in conjunction with the Los Alamos IGPP workshop on mantle convection.

REFERENCES

BAUMGARDNER, J. R. 1985 Three-dimensional treatment of convective flow in the Earth's mantle. *J. Statist. Phys.* **39**, 501–511.

BERCOVICI, D., SCHUBERT, G., GLATZMAIER, G. & ZEBIB, A. 1989 Three-dimensional thermal convection in a spherical shell. *J. Fluid Mech.* **206**, 75–104.

BOLTON, E. W. & BUSSE, F. H. 1985 Stability of convection rolls in a layer with stress-free boundaries. *J. Fluid Mech.* **150**, 487–498.

BUSSE, F. H. 1967*a* On the stability of two-dimensional convection in a layer heated from below. *J. Maths Phys.* **46**, 140–150.

BUSSE, F. H. 1967*b* The stability of finite amplitude cellular convection and its relation to an extremum principle. *J. Fluid Mech.* **30**, 625–649.

BUSSE, F. H. 1981 Transition to turbulence in Rayleigh–Bénard convection. In *Hydrodynamic Instabilities and the Transition to Turbulence* (ed. H. L. Swinney & J. P. Gollup), pp. 97–137. Springer.

BUSSE, F. H. & WHITEHEAD, J. A. 1971 Instability of convection rolls in a high Prandtl number fluid. *J. Fluid Mech.* **47**, 305–320.

CHRISTENSEN, U. 1987 Time-dependent convection in elongated Rayleigh–Bénard cells. *Geophys. Res. Lett.* **14**, 220–223.

CLEVER, R. M. & BUSSE, F. H. 1989 Three-dimensional knot convection in a layer heated from below. *J. Fluid Mech.* **198**, 345–363.

CSEREPES, L., RABINOWICZ, M. & ROSENBERG-BOROT, C. 1988 Three-dimensional convection in a two-layer mantle. *J. Geophys. Res.* **93**, 12009–12025.

CURRY, J. H., HERRING, J. R. & ORSZAG, S. A. 1984 Order and disorder in two- and three-dimensional Bénard convection. *J. Fluid Mech.* **147**, 1–38.

FRICK, H., BUSSE, F. H. & CLEVER, R. M. 1983 Steady three-dimensional convection at high Prandtl number. *J. Fluid Mech.* **127**, 141–153.

GLATZMAIER, G. A. 1989 Numerical simulations of mantle convection: time-dependent three-dimensional compressible, spherical shell. *Geophys. Astrophys. Fluid Dyn.* **43**, 223–264.

GRÖTZBACH, G. 1982 Direct numerical simulation of laminar and turbulent Bénard convection. *J. Fluid Mech.* **119**, 27–53.

HOUSEMAN, G. 1988 The dependence of convection planform on mode of heating. *Nature* **332**, 346–349.

MACHETEL, P., RABINOWICZ, M. & BERNARDET, P. 1986 Three-dimensional convection in spherical shells. *Geophys. Astrophys. Fluid Dyn.* **37**, 57–84.

MACHETEL, P. & YUEN, D. A. 1987 Chaotic axisymmetrical spherical convection and large-scale mantle circulation. *Earth Planet. Sci. Lett.* **86**, 93–104.

MALKUS, W. V. R. & VERONIS, G. 1958 Finite amplitude cellular convection. *J. Fluid Mech.* **4**, 225–260.

OLIVER, D. S. & BOOKER, J. R. 1983 Planform and heat transport of convection with strongly temperature-dependent viscosity. *Geophys. Astrophys. Fluid Dyn.* **27**, 73–85.

PALM, E. 1960 On the tendency towards hexagonal cells in steady convection. *J. Fluid Mech.* **8**, 183–192.

RAMSHAW, J. & DUKOWICZ, J. 1979 APACHE: A generalized-mesh Eulerian computer code for multicomponent chemically reactive fluid flow. *Los Alamos Natl. Lab. Rep.* LA-7427.

SCHNAUBELT, M. & BUSSE, F. H. 1989 On the stability of two-dimensional convection rolls in an infinite Prandtl number fluid with stress-free boundaries. *Z. Angew. Math. Phys.* **40**, 153–162.

SCHUBERT, G. & ANDERSON, C. A. 1985 Finite element calculations of very high Rayleigh number thermal convection. *Geophys. J. R. Astron. Soc.* **80**, 575–601.

STRAUS, J. M. 1972 Finite amplitude doubly diffusive convection. *J. Fluid Mech.* **56**, 353–374.

SWEET, R. 1977 A cyclic reduction algorithm for solving block tridiagonal systems of arbitrary dimensions. *SIAM J. Anal.* **14**, 706–720.

WHITE, D. B. 1988 The planforms and onset of convection with a temperature-dependent viscosity. *J. Fluid Mech.* **191**, 247–286.

WHITEHEAD, J. A. & PARSONS, B. 1978 Observations of convection at Rayleigh numbers up to 760,000 in a fluid with large Prandtl number. *Geophys. Astrophys. Fluid Dyn.* **9**, 201–217.

ZEBIB, A., GOYAL, A. K. & SCHUBERT, G. 1985 Convective motions in a spherical shell. *J. Fluid Mech.* **152**, 39–48.